

Turbulence-Induced 2D Correlated Image Distortion

Armin Schwartzman
Div. Biostatistics
UC San Diego
La Jolla, CA, USA
armins@ucsd.edu

Marina Alterman
Dept. Elect. Eng. & Comp. Sci.
Northwestern University
Evanston, IL, USA
marina.alterman@northwestern.edu

Rotem Zamir, Yoav Y. Schechner
Viterbi Faculty of Electrical Eng.
Technion - Israel Inst. Technology
Haifa, Israel
ratume@campus.technion.ac.il
yoav@ee.technion.ac.il

Abstract

Due to atmospheric turbulence, light randomly refracts in three dimensions (3D), eventually entering a camera at a perturbed angle. Each viewed object point thus has a distorted projection in a two-dimensional (2D) image. Simulating 3D random refraction for all viewed points via complex simulated 3D random turbulence is computationally expensive. We derive an efficient way to render 2D image distortions, consistent with turbulence. Our approach bypasses 3D numerical calculations altogether. We directly create 2D random physics-based distortion vector fields, where correlations are derived in closed form from turbulence theory. The correlations are nontrivial: they depend on the perturbation directions relative to the orientation of all object-pairs, simultaneously. Hence, we develop a theory characterizing and rendering such a distortion field. The theory is turned to a few simple 2D operations, which render images based on camera and atmospheric properties.

1. Introduction

Imaging through refractive media [5, 6, 25, 40, 42, 45] is of interest both for rendering [11, 47, 58] and scene analysis [2, 27, 37, 54, 56]. It is studied in computer vision and graphics, as the importance of participating media is acknowledged [3, 8, 16, 18, 22, 24, 35, 36, 41, 46, 49, 55]. Complex, random refraction is created by turbulent media [13, 17, 29], often encountered in long range observations through the atmosphere [23, 28, 48, 57] and ground-based astronomy [39, 44]. There, random perturbations of the refractive index [38] follow a complicated fractal multi-scale structure of eddies in the three dimensional (3D) domain. This structure, in turn, creates highly complex refraction of propagating light, in the 5D plenoptic domain (space and direction). This leads to random perturbations

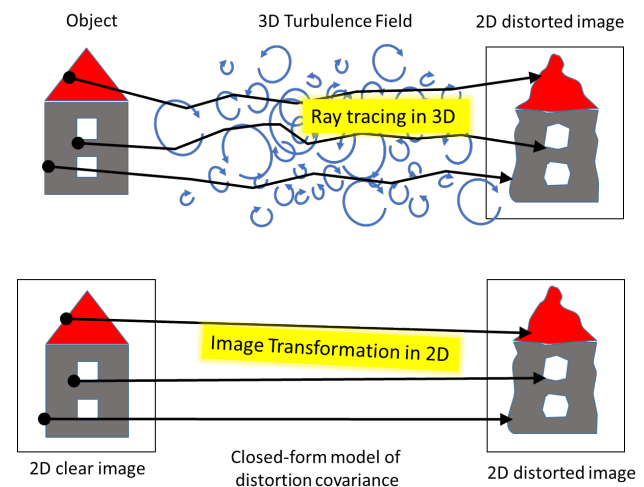


Figure 1: [Top] Computationally complex rendering of image distortion, requiring a 3D simulated random turbulent field, then ray tracing in 3D for all object points in the field of view. [Bottom] Our approach. Efficient rendering of turbulence-induced distortion as 2D image processing. It relies on closed-form physics-based covariance of the distortion.

of all light rays passing through this medium. Finally, the complexly refracted light is projected by a camera, forming a distorted image of the scene.

Now, suppose one seeks to render images that are distorted as if they are taken through atmospheric turbulence. A motivation for rendering can be computer graphics. Another motivation is to form a database on which to test and develop recovery algorithms, to correct for turbulence-induced distortion [60, 61]. A database can also train a learning system to recognize objects via turbulence. From the description above, apparently, rendering should include a series of computationally complex steps (Fig. 1[Top]):

Simulate a huge 3D turbulent random field (scale of kilometers) at a 3D resolution that is relevant to optics; Ray-

trace refraction through this 3D medium, from an object point to the camera; Repeat this propagation process for *all* resolvable points in the field of view. In large scales, such a rendering approach poses a computational burden. It is also unnecessary.

We believe that for some applications, there is *no need for 3D simulations*, in order to render turbulence-induced image distortion. There is no need to simulate a fractal random refractive index 3D field, or ray-trace through such a field. Basically, image distortion is an operation in just *two dimensions* (2D). The input is a 2D image, free of random distortion, i.e. the view in the absence of turbulence. The output is a 2D distorted image (Fig. 1[Bottom]). Rendering boils down, thus, to creating a 2D distortion operation, which is consistent with distortion that turbulence can induce.

Random 3D turbulence eventually leads to a randomly distorted 2D projection. The random distorted projection must be drawn from a distribution that is characterised by a covariance function. The covariance function determines how the distortion of any pixel is correlated to any other pixel, and what the variance is. The covariance function of turbulence-induced distortion is *defined by physics*. In other words, the physics of turbulence in 3D (a random process), and 5D refraction in it, dictate the image-distortion covariance function, in 2D. The probability distribution of distortion had already been derived using the theory of turbulence, *for pairs of object points* (not full-field images) [7, 51]. This pair-wise function had also been verified empirically, using field experiments [7], where correlations between image points were measured. We thus use the pair-wise covariance function of turbulence-induced image distortion, to create 2D distortion fields.

Transferring the physics-based pair-wise covariance function to a full distortion field is nontrivial in turbulence. Distortion is a vector-valued spatial field. The covariance of this field is a matrix-valued function. It is a function of relative coordinates that vary *for each pair* of pixels, including the relative orientation of each pair, and the distortion orientation in each pixel. We derive theoretically the solution: a full-field covariance of a 2D distortion field, based on the physics-based pair-wise orientation-sensitive covariance. We then give a recipe how to render random 2D distortion fields that satisfy the physical model. The recipe is composed of several simple 2D image operations.

2. Related Work

2.1. Phase Screen Propagation

A common method for simulating imaging through turbulence is based on light propagation through multiple random 2D phase screens [33], approximating a 3D turbulent medium. Phase-shifting layers are generated using ei-

ther fast Fourier transform (FFT), the Zernike polynomial method or the fractal interpolation method [59]. This approach requires simulating a 3D refractive field and light propagation in 3D.

2.2. 3D Ray Tracing for Graphics

There are rendering techniques that trace rays through a 3D randomly refractive media. Physically based simulation of atmospheric phenomena is done in [19, 20]. Rendering complicated lighting effects through various refractive objects is presented in [26]. These 3D methods often require specialized hardware such as GPU and extensive computation time.

2.3. 2D Image Distortion Simulation

2D image distortion is simpler to implement, and does not require extensive computational power. Usually, parametric models are used. These models are based on analysis of real empirical distortions observed through various atmospheric conditions [15, 43]. Other methods, as in [14, 61], use simple Gaussian random functions to generate image distortion fields. The results resemble turbulence distortion. However, these methods do not use a physical model and are not set to have physically consistent spatial correlations.

3. Background

3.1. Turbulence and Variance

3D turbulent flow is characterized by independent fluid eddies in a range of scales. An eddy at the largest (outer) spatial scale L_0 break into smaller eddies, which in turn break further. The process continues until the smallest eddies reach the inner scale of the turbulence, l_0 . The *inertial range* is defined by $[l_0, L_0]$. There, kinetic energy is transferred to eddies of decreasing scale. Below l_0 , energy in the fluid motion dissipates fully into heat. The outer scale of the turbulence is often modelled [52] as $L_0 = 0.4h$, where h is the height above ground.

A turbulent flow is accompanied by pressure and temperature fluctuations, that affects the refractive index of the medium [4, 32]. In statistically homogeneous and locally isotropic turbulence [30, 31] refractive fluctuations are characterized by a refractive index *structure constant* C_n^2 . It expresses turbulence strength [1, 53] and measured in units of $m^{-2/3}$. A high value of C_n^2 indicates strong turbulence, while $C_n^2 = 0$ represents a medium free of turbulence. In air, C_n^2 is typically the range $10^{-17} - 10^{-13} m^{-2/3}$. A high value of 8×10^{-13} is typical [1] of summer daytime. Since turbulence strength depends on the environment, in general C_n^2 can vary over the imaging path. In particular it is affected by high pressure at low altitudes and strong winds at high altitudes, both of which affect placement and performance of sky-observing telescopes. In this paper, we focus

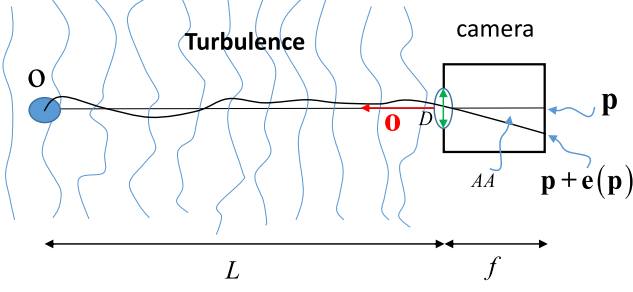


Figure 2: Without turbulence, the line of sight to an object point o is \mathbf{o} . The point is projected then to \mathbf{p} . Here L is the path length, f is focal length and D is the lens aperture diameter. Random refractions in the turbulent medium creates an angle of arrival (AA) perturbation, leading to a distorted projection to $\mathbf{p} + \mathbf{e}(\mathbf{p})$.

on rather horizontal views, which are typical in applications such as long distance observations.

A camera having focal length f observes an object point o at distance L . Without turbulence, the line of sight is expressed by unit vector \mathbf{o} . As illustrated in Fig. 2, due to refractive index fluctuations, turbulence leads to random refraction of light emanating from the object point. Thus, this light arrives at the camera at a random angle of arrival (AA), which is a perturbation around the direction of \mathbf{o} . The AA perturbation distorts the projection of o at the image plane.

The AA variance for a spherical light wavefront¹ is [10]:

$$\sigma_{AA}^2 = \gamma(q) \mathcal{C}_n^2 L D^{-1/3}, \quad (1)$$

where D is the diameter of the camera lens and q is the Fresnel number:

$$q = \frac{D}{\sqrt{\lambda L}}. \quad (2)$$

Here λ is the light wavelength. The coefficient $\gamma(q)$ for a spherical wave [10] is

$$\gamma(q) = \frac{\sqrt{3}}{16} \Gamma\left(\frac{1}{6}\right) \Gamma\left(\frac{8}{3}\right) \left(\frac{2}{\beta}\right)^{\frac{1}{3}} \left[1 + \frac{6}{17} \frac{8}{3} \cdot \operatorname{Re} \left\{ \left(-\frac{\pi(\beta q)^2}{2j} \right)^{\frac{1}{6}} {}_2F_1 \left(\frac{1}{6}, \frac{17}{6}; \frac{23}{6}; 1 + \frac{\pi(\beta q)^2}{2j} \right) \right\} \right] \quad (3)$$

where $\beta = 0.5216$ and

$$\Gamma(\mu) = \int_0^\infty \tau^{\mu-1} e^{-\tau} d\tau \quad (4)$$

is the Gamma function. In Eq. (3), ${}_2F_1(\cdot)$ is the hypergeometric function

$${}_2F_1(a, d; c; \zeta) = \sum_{m=0}^{\infty} \frac{(a)_m (d)_m}{(c)_m} \frac{\zeta^m}{m!}. \quad (5)$$

¹We deal with light emanating from an object point. Light from different object points is assumed to be incoherent. Hence, light from any observed object point is modelled as having a spherical wavefront.

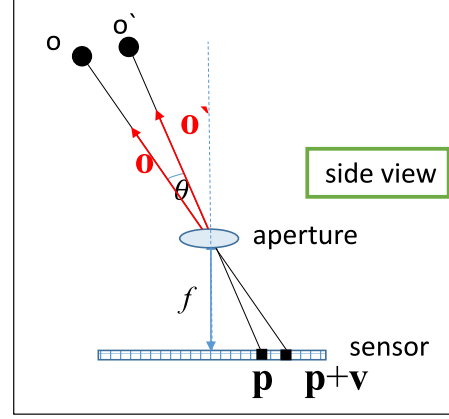


Figure 3: Without turbulence, the lines of sight to two object points o, o' are respectively \mathbf{o}, \mathbf{o}' . The points then project to \mathbf{p} and $\mathbf{p} + \mathbf{v}$, respectively.

For $q \gg 1$, Eq. (3) simplifies [12] to

$$\gamma(q) \approx 1.09. \quad (6)$$

3.2. Pair-wise Distortion Correlation

Now, consider *two object points*, o, o' . Without turbulence, their corresponding lines of sight are defined by unit vectors \mathbf{o}, \mathbf{o}' , from the camera's center of projection, as can be seen in Fig. 3. These lines form a plane $\Pi = \mathbf{o} \times \mathbf{o}'$. The angle between them is

$$\theta = \arccos(\mathbf{o} \cdot \mathbf{o}') . \quad (7)$$

Turbulence-induced random refractive disturbance causes each of these lines of sight to deviate, correspondingly, by angles of arrival $AA(o), AA(o')$. There is correlation between $AA(o), AA(o')$. The AA correlation function is

$$b(\theta) = \frac{\operatorname{Cov}[AA(o), AA(o')]}{\sigma_{AA}^2}, \quad (8)$$

where Cov is the covariance operation. An expression for $b(\theta)$ is derived in Refs. [7] and [51]. The correlation generally decreases with θ . Moreover, the correlation *depends on the directions* of the AAs, relative to Π . Suppose an AA perturbation is within the plane Π , which includes \mathbf{o}, \mathbf{o}' . Then, this perturbation is termed *parallel* and denoted \parallel . If an AA perturbation is *perpendicular* to this plane, it is denoted \perp . In general, an AA perturbation at o has both parallel and perpendicular components.

Note that for a fixed o , the \parallel, \perp axes and components are defined *depending on another point* o' . Since object point o coexists with a large number W of other points in various relative directions, there are $\mathcal{O}(W)$ definitions of \parallel, \perp for any particular o . We deal, thus, with a non-trivial field.

Let us return, for the moment, to analyzing two particular object points o, o' . Use the following dimensionless variables. From the object's point of view, the angular size of the aperture is

$$\theta_D = \frac{D}{L}. \quad (9)$$

The inter-object view angle is normalized to

$$\eta = \frac{\theta}{\theta_D}. \quad (10)$$

The outer scale of the turbulence is normalized to

$$\rho = \frac{L_0}{D}. \quad (11)$$

For the dimensionless parameter $0 \leq \xi \leq 1$, define the functions

$$Q(\xi) = (1 - \xi)^{5/3}, \quad M_\eta = 2\eta\xi(1 - \xi). \quad (12)$$

Following Ref. [7], the correlation function of each of the two components is

$$b_{\parallel, \perp}(\eta) = \frac{\int_0^1 \left\{ \int_0^\infty H(\kappa) [J_0(M_\eta \kappa) \mp J_2(M_\eta \kappa)] d\kappa \right\} C_n^2(L\xi) Q(\xi) d\xi}{\int_0^1 \left\{ \int_0^\infty H(\kappa) d\kappa \right\} C_n^2(L\xi) Q(\xi) d\xi} \quad (13)$$

Here, κ is a dimensionless integration variable included in real non negative numbers, C_n^2 is the refractive index structure constant (see Sec. 3.1), J_0 and J_2 are Bessel functions of the first kind, while

$$H(\kappa) = \frac{[(2\rho\kappa)^2 + 1]^{-11/6} J_2^2(\kappa)}{\kappa}. \quad (14)$$

The negative sign in Eq. (13) corresponds to $b_{\parallel}(\eta)$, while the positive sign corresponds $b_{\perp}(\eta)$. Notice that the denominator of (13) is simply the numerator evaluated at $\eta = 0$, so that $b_{\parallel, \perp}(0) = 1$.

In a horizontal path, for which C_n^2 is constant, Eq. (13) simplifies to

$$b_{\parallel, \perp}(\eta) = \frac{\int_0^1 \left\{ \int_0^\infty H(\kappa) [J_0(M_\eta \kappa) \mp J_2(M_\eta \kappa)] d\kappa \right\} Q(\xi) d\xi}{\int_0^1 \left\{ \int_0^\infty H(\kappa) d\kappa \right\} Q(\xi) d\xi} \quad (15)$$

The correlation function (15) no longer depends on C_n^2 nor on the range L , but depends on ρ and η . The correlation function (15) can be easily computed, as plotted in Fig. 4.

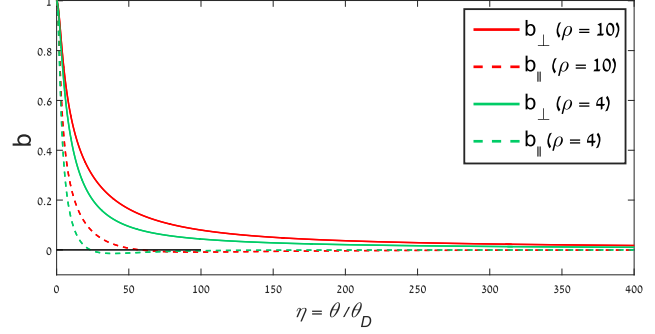


Figure 4: The correlation function (15) between a pair of pixels, for the two distortion components (\parallel, \perp), plotted for $\rho = 4$ and $\rho = 10$.

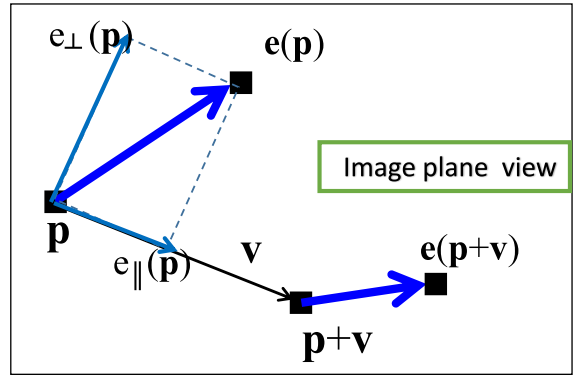


Figure 5: The image plane. In absence of distortion, two object points project to \mathbf{p} and $\mathbf{p} + \mathbf{v}$. Turbulence induces projection displacements, $\mathbf{e}(\mathbf{p})$ and $\mathbf{e}(\mathbf{p} + \mathbf{v})$, respectively. Any displacement vector $\mathbf{e}(\mathbf{p})$ can be divided to components parallel and perpendicular to \mathbf{v} . These components are denoted $e_{\parallel}(\mathbf{p})$, $e_{\perp}(\mathbf{p})$.

4. Designing the Field Autocorrelation

4.1. Autocorrelation of a Stationary Vector Field

In this section, we work directly in the 2D image domain. We define the distortion vector field, and a matrix-valued covariance function in this field. Consider Fig. 5. Image pixel location \mathbf{p} is the undistorted projection of \mathbf{o} . Without turbulence, the line of sight \mathbf{o}' from object o' projects to 2D pixel location $\mathbf{p} + \mathbf{v}$. Turbulence displaces the respective projections by the random vectors $\mathbf{e}(\mathbf{p})$ and $\mathbf{e}(\mathbf{p} + \mathbf{v})$. Hence, \mathbf{e} is a random *vector field* in the image plane. All vectors, \mathbf{p} , \mathbf{v} , \mathbf{e} are given in the (x, y) coordinates of the image domain. Specifically, the cartesian components of \mathbf{v} are v_x, v_y . All spatial components, as well as the focal length f have pixel-units. For narrow view angles,

$$\theta \approx \frac{|\mathbf{v}|}{f} = \frac{r}{f}, \quad (16)$$

where $r = |\mathbf{v}|$. Thus, referring to Eqs. (10,15),

$$b_{\parallel,\perp}(\eta) = b_{\parallel,\perp} \left(\frac{r}{f\theta_D} \right). \quad (17)$$

To simulate a turbulence distorted image, we seek a random field \mathbf{e} with correct spatial correlations. The displacement \mathbf{e} is a spatially stationary vector field with mean zero. Since we are interested in the autocorrelation function of this field, we may assume without loss of generality that the variance of \mathbf{e} is 1: the variance can be adjusted later as needed, using Eq. (1). The autocorrelation is equal to the auto-covariance function and is given by the 2×2 matrix

$$\mathbf{C}(\mathbf{v}) = E [\mathbf{e}(\mathbf{p})\mathbf{e}^T(\mathbf{p} + \mathbf{v})]. \quad (18)$$

Here E denotes expectation and T denotes transposition. Note that $\mathbf{C}(\mathbf{v})$ is a *matrix-valued* function of v_x, v_y . By the stationarity assumption, the autocorrelation function depends only on the difference \mathbf{v} between two points and it is symmetric in the sense that $\mathbf{C}(-\mathbf{v}) = \mathbf{C}^T(\mathbf{v})$.

We wish to find a correlation function (18) such that the induced longitudinal and lateral autocorrelation functions match Eq. (15). Define the unit vector

$$\hat{\mathbf{v}} = \mathbf{v}/r. \quad (19)$$

From Fig. 5, the longitudinal component of the displacement vector field $\mathbf{e}(\mathbf{p})$ is the projection of $\mathbf{e}(\mathbf{p})$ onto $\hat{\mathbf{v}}$:

$$e_{\parallel}(\mathbf{p}) = \langle \hat{\mathbf{v}}, \mathbf{e}(\mathbf{p}) \rangle = \hat{\mathbf{v}}^T \mathbf{e}(\mathbf{p}), \quad (20)$$

where $\langle \cdot, \cdot \rangle$ is the inner product operator. Let

$$\mathbf{R} = \begin{pmatrix} 0 & -1 \\ 1 & 0 \end{pmatrix} \quad (21)$$

denote a rotation matrix, which rotates \mathbf{v} by 90° in the image plane. Thus

$$\hat{\mathbf{v}}^T \mathbf{R} \hat{\mathbf{v}} = 0. \quad (22)$$

The perpendicular displacement $e_{\perp}(\mathbf{p})$ is the projection of $\mathbf{e}(\mathbf{p})$ onto the perpendicular vector $\mathbf{R}\hat{\mathbf{v}}$:

$$e_{\perp}(\mathbf{p}) = \langle \mathbf{R}\hat{\mathbf{v}}, \mathbf{e}(\mathbf{p}) \rangle = \hat{\mathbf{v}}^T \mathbf{R}^T \mathbf{e}(\mathbf{p}). \quad (23)$$

From Eq. (18), the autocorrelation scalar functions of the parallel and perpendicular displacements are, respectively

$$C_{\parallel}(\mathbf{v}) = E [e_{\parallel}(\mathbf{p})e_{\parallel}^T(\mathbf{p} + \mathbf{v})] = E [\hat{\mathbf{v}}^T \mathbf{e}(\mathbf{p}) \mathbf{e}^T(\mathbf{p} + \mathbf{v}) \hat{\mathbf{v}}] = \hat{\mathbf{v}}^T \mathbf{C}(\mathbf{v}) \hat{\mathbf{v}} \quad (24)$$

$$C_{\perp}(\mathbf{v}) = E [e_{\perp}(\mathbf{p})e_{\perp}^T(\mathbf{p} + \mathbf{v})] = \hat{\mathbf{v}}^T \mathbf{R}^T \mathbf{C}(\mathbf{v}) \mathbf{R} \hat{\mathbf{v}}. \quad (25)$$

4.2. A Solution to the Autocorrelation Function

Given parallel and perpendicular autocorrelation scalar functions $C_{\parallel}(\mathbf{v})$ and $C_{\perp}(\mathbf{v})$, we seek a matrix-valued autocorrelation function $\mathbf{C}(\mathbf{v})$ that is consistent with Eq. (24) and Eq. (25), respectively. The solution to such a problem is not unique. Let us use the solution class:

$$\mathbf{C}(\mathbf{v}) = A(\mathbf{v})\mathbf{I} - B(\mathbf{v})\hat{\mathbf{v}}\hat{\mathbf{v}}^T, \quad (26)$$

where $A(\mathbf{v}), B(\mathbf{v})$ are scalar functions and \mathbf{I} is the 2×2 identity matrix. In the class defined by Eq. (26), parallel and perpendicular displacements are uncorrelated. Indeed, using (26),

$$E [e_{\parallel}(\mathbf{p})e_{\perp}^T(\mathbf{p} + \mathbf{v})] = E [\hat{\mathbf{v}}^T \mathbf{e}(\mathbf{p})\mathbf{e}^T(\mathbf{p} + \mathbf{v})\mathbf{R}\hat{\mathbf{v}}] = \hat{\mathbf{v}}^T \mathbf{C}(\mathbf{v}) \mathbf{R} \hat{\mathbf{v}} = \hat{\mathbf{v}}^T A(\mathbf{v}) \mathbf{R} \hat{\mathbf{v}} - \hat{\mathbf{v}}^T B(\mathbf{v}) \hat{\mathbf{v}} \hat{\mathbf{v}}^T \mathbf{R} \hat{\mathbf{v}} = 0, \quad (27)$$

where we have used Eq. (22) and the scalar-valued nature of the functions $A(\mathbf{v})$ and $B(\mathbf{v})$.

To determine the required functions A, B , we substitute Eq. (26) into Eqs. (24) and (25), yielding

$$C_{\parallel}(\mathbf{v}) = A(\mathbf{v})\hat{\mathbf{v}}^T \hat{\mathbf{v}} - B(\mathbf{v})(\hat{\mathbf{v}}^T \hat{\mathbf{v}})^2 = A(\mathbf{v}) - B(\mathbf{v}) \quad (28)$$

$$C_{\perp}(\mathbf{v}) = A(\mathbf{v})\hat{\mathbf{v}}^T \mathbf{R}^T \mathbf{R} \hat{\mathbf{v}} - B(\mathbf{v})\hat{\mathbf{v}}^T \mathbf{R}^T \hat{\mathbf{v}} \hat{\mathbf{v}}^T \mathbf{R} \hat{\mathbf{v}} = A(\mathbf{v}). \quad (29)$$

Here we used $\mathbf{R}^T \mathbf{R} = \mathbf{I}$ and Eq. (22). Eqs. (26,28,29) yield

$$\mathbf{C}(\mathbf{v}) = C_{\perp}(\mathbf{v})\mathbf{I} - [C_{\perp}(\mathbf{v}) - C_{\parallel}(\mathbf{v})] \hat{\mathbf{v}}\hat{\mathbf{v}}^T. \quad (30)$$

4.3. Consistency with Turbulence Correlation

Given Eqs. (10,15,17), the parallel and perpendicular scalar autocorrelation functions must be set to satisfy

$$C_{\parallel}(\mathbf{v}) = b_{\parallel} \left(\frac{r}{f\theta_D} \right), \quad C_{\perp}(\mathbf{v}) = b_{\perp} \left(\frac{r}{f\theta_D} \right). \quad (31)$$

Thus, the desired autocorrelation function can be written as

$$\mathbf{C}(\mathbf{v}) = A(r)\mathbf{I} - B(r)\hat{\mathbf{v}}\hat{\mathbf{v}}^T \quad (32)$$

using the positive functions

$$A(r) = b_{\perp} \left(\frac{r}{f\theta_D} \right) \\ B(r) = b_{\perp} \left(\frac{r}{f\theta_D} \right) - b_{\parallel} \left(\frac{r}{f\theta_D} \right). \quad (33)$$

In a 2D spatial image domain of size $U \times U$, the autocorrelation domain \mathbf{v} has size $2U \times 2U$.

We show an example using the following parameters: $\lambda = 550\text{nm}$, pixel size $4\mu\text{m}$, $U = 1024$ pixels, Nikon AF-S Nikkor lens, with $f = 300\text{mm}$ and $f\# = 5.6$, at height $h = 4\text{m}$. Object distance is $L = 2\text{km}$ and

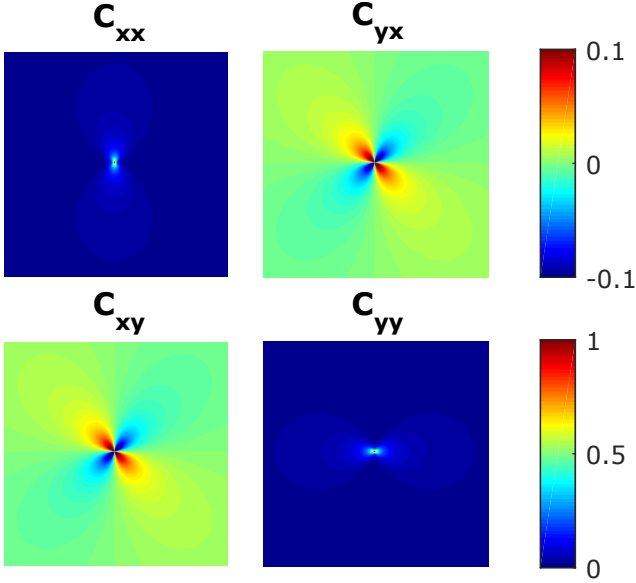


Figure 6: The 2×2 matrix-valued $\mathbf{C}(\mathbf{v})$, based on parameters of the example detailed in Sec. 4.3. In each sub-plot, the spatial dimensions of the \mathbf{v} domain are 2048×2048 pixels, corresponding to an image of size 1024×1024 . The top-right scale-bar corresponds to C_{xy}, C_{yx} , having negative as well as positive values. The bottom-right scale-bar corresponds to C_{xx}, C_{yy} , having non-negative values.

$\mathcal{C}_n^2 = 3.6 \cdot 10^{-13} \text{m}^{-2/3}$. The AA variance and correlation are then calculated using Eqs. (9-15). Figs. 6 and 7 plot each element of the 2×2 matrix $\mathbf{C}(\mathbf{v})$, as a function of \mathbf{v} . Using the same fixed imaging parameters, this example is further followed in this paper when creating Figs. 8,9,10,13, as explained next.

5. Creating a Distortion Field

In this section, we derive a recipe for creating a random distortion field $\mathbf{e}(\mathbf{p})$, whose auto-correlation is consistent with $\mathbf{C}(\mathbf{v})$, given in Eqs. (32,33). Some of the expressions here are matrix-valued generalizations of simple, textbook relations of scalar-valued fields.

Let $\mathbf{z}(\mathbf{p})$ be a white noise vector field such that each element in it is a 2×1 vector and $E[\mathbf{z}(\mathbf{p})\mathbf{z}^T(\mathbf{p} + \mathbf{v})] = \mathbf{I}\delta(\mathbf{v})$. A random vector field having an autocorrelation function $\mathbf{C}(\mathbf{v})$ can be obtained by a convolution of $\mathbf{z}(\mathbf{p})$ with a deterministic matrix-valued kernel $\mathbf{K}(\mathbf{p})$:

$$\mathbf{e}(\mathbf{p}) = \int \mathbf{K}(\mathbf{p} - \mathbf{p}')\mathbf{z}(\mathbf{p}')d\mathbf{p}'. \quad (34)$$

Here $\mathbf{K}(\mathbf{p})$ is a matrix-valued field: there is a 2×2 matrix $\mathbf{K}(\mathbf{p})$ for each vector \mathbf{p} . The goal is to find a kernel $\mathbf{K}(\mathbf{p})$ such that the field $\mathbf{e}(\mathbf{p})$ has the desired autocorrelation function $\mathbf{C}(\mathbf{v})$, given in Eqs (32,33).

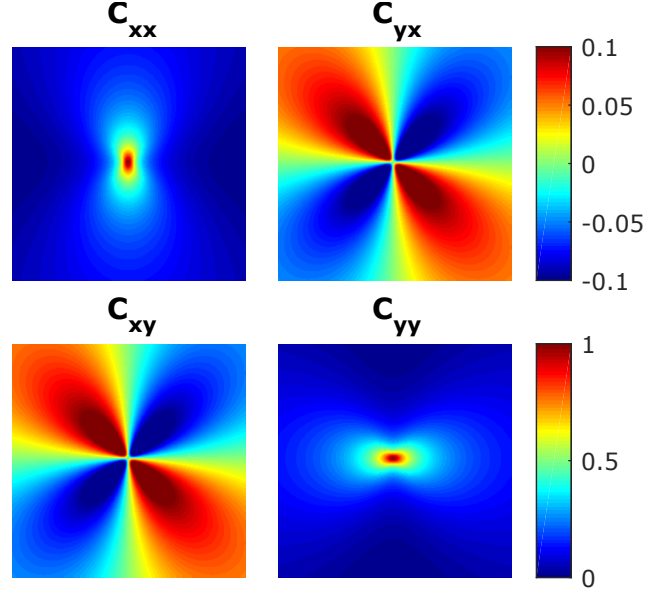


Figure 7: A 10×10 zoom-in on $\mathbf{C}(\mathbf{v})$ of Fig. 6.

The 2×2 matrix-valued autocorrelation function $\mathbf{C}(\mathbf{v})$ is related to the 2×2 matrix-valued convolution kernel $\mathbf{K}(\mathbf{p})$, through

$$\mathbf{C}(\mathbf{v}) = \int \mathbf{K}(\mathbf{p})\mathbf{K}^T(\mathbf{p} + \mathbf{v})d\mathbf{p}. \quad (35)$$

Deriving $\mathbf{K}(\mathbf{p})$ based on Eq. (35) is a deconvolution problem. This deconvolution can be solved in the Fourier domain. Let $\boldsymbol{\omega}$ be a 2D spatial frequency vector. From (34), the spatial Fourier transform of the vector field $\mathbf{e}(\mathbf{p})$ is the vector field

$$\tilde{\mathbf{e}}(\boldsymbol{\omega}) = \int \mathbf{e}(\mathbf{p})e^{-j\boldsymbol{\omega}^T\mathbf{p}}d\mathbf{p} = \tilde{\mathbf{K}}(\boldsymbol{\omega})\tilde{\mathbf{z}}(\boldsymbol{\omega}). \quad (36)$$

On the other hand, the spatial Fourier transform of $\mathbf{C}(\mathbf{v})$ is the matrix-valued spectral density function

$$\tilde{\mathbf{C}}(\boldsymbol{\omega}) = \int \mathbf{C}(\mathbf{v})e^{-j\boldsymbol{\omega}^T\mathbf{v}}d\mathbf{v} = E[\tilde{\mathbf{e}}^*(\boldsymbol{\omega})\tilde{\mathbf{e}}^T(\boldsymbol{\omega})], \quad (37)$$

where $*$ denotes the complex conjugation. There is a 2×2 matrix $\tilde{\mathbf{C}}(\boldsymbol{\omega})$ for each $\boldsymbol{\omega}$. Substituting Eq. (36) into Eq. (37):

$$\begin{aligned} \tilde{\mathbf{C}}(\boldsymbol{\omega}) &= E[\tilde{\mathbf{K}}^*(\boldsymbol{\omega})\tilde{\mathbf{z}}^*(\boldsymbol{\omega})\tilde{\mathbf{z}}^T(\boldsymbol{\omega})\tilde{\mathbf{K}}^T(\boldsymbol{\omega})] \\ &= \tilde{\mathbf{K}}^*(\boldsymbol{\omega})E[\tilde{\mathbf{z}}^*(\boldsymbol{\omega})\tilde{\mathbf{z}}^T(\boldsymbol{\omega})]\tilde{\mathbf{K}}^T(\boldsymbol{\omega}) = \tilde{\mathbf{K}}^*(\boldsymbol{\omega})\tilde{\mathbf{K}}^T(\boldsymbol{\omega}). \end{aligned} \quad (38)$$

Eq. (38) uses the fact that the spectral density of any white noise field is $E[\tilde{\mathbf{z}}^*(\boldsymbol{\omega})\tilde{\mathbf{z}}^T(\boldsymbol{\omega})] = \mathbf{I}, \forall \boldsymbol{\omega}$. Eq. (38) is thus the spatial Fourier transform of (35).

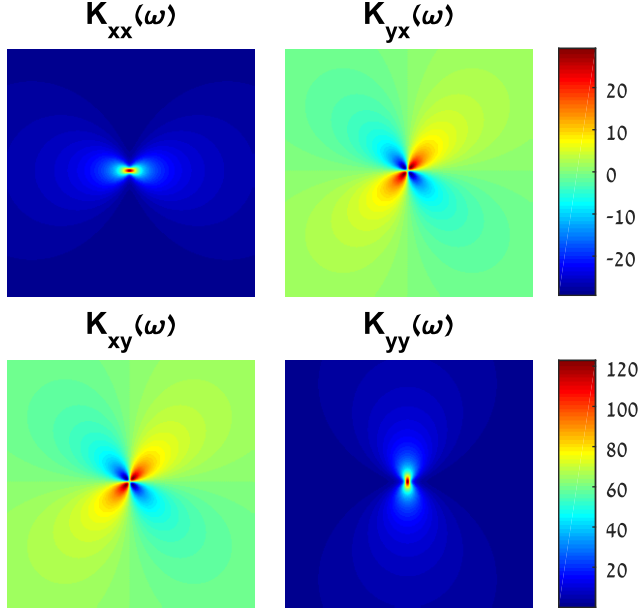


Figure 8: The 2×2 matrix-valued $\tilde{\mathbf{K}}(\omega)$, that corresponds to the function $\mathbf{C}(\mathbf{v})$ shown in Figs. 6,7. It was calculated using FFT, as described in Sec. 6. The plots here are a $\times 10$ zoom-in on the low-frequency domain. The top-right scale-bar corresponds to $\tilde{K}_{xy}, \tilde{K}_{yx}$. The bottom-right scale-bar corresponds to $\tilde{K}_{xx}, \tilde{K}_{yy}$.

The autocorrelation function $\mathbf{C}(\mathbf{v})$ is real, symmetric as a matrix, symmetric with respect to sign changes of its argument \mathbf{v} and its diagonal entries are positive definite functions. As a result, its Fourier transform $\tilde{\mathbf{C}}(\omega)$ is also real, symmetric as a matrix, symmetric with respect to sign changes of its argument ω , and its diagonal entries are positive functions. While there are many 2×2 matrices $\tilde{\mathbf{K}}$ satisfying (38), it is natural to choose the symmetric square root of $\tilde{\mathbf{C}}(\omega)$, which enjoys the same properties. Given $\tilde{\mathbf{C}}(\omega)$, its matrix square root can be computed per ω using the formula [34]:

$$\tilde{\mathbf{K}}(\omega) = \frac{1}{t(\omega)} \left[\tilde{\mathbf{C}}(\omega) + s(\omega)\mathbf{I} \right]. \quad (39)$$

Here $s(\omega) = \sqrt{\det \tilde{\mathbf{C}}(\omega)}$ and $t(\omega) = \sqrt{\text{tr} \tilde{\mathbf{C}}(\omega) + 2s(\omega)}$. For example, Fig. 8 plots each element of the 2×2 matrix $\tilde{\mathbf{K}}(\omega)$, as a function of ω , in correspondence with the function $\mathbf{C}(\mathbf{v})$ shown in Figs. 6,7.

To generate a random field $\mathbf{e}(\mathbf{p})$ with cross-spectral density $\tilde{\mathbf{C}}(\omega)$, it is not actually necessary to find $\tilde{\mathbf{K}}(\omega)$, the inverse Fourier transform of $\tilde{\mathbf{K}}(\omega)$. It suffices to do the filtering in the Fourier domain, similarly to [50]. The theoretical recipe is thus:

- 1 Calculate $\mathbf{C}(\mathbf{v})$ using Eqs (32,33).
- 2 Fourier transform $\mathbf{C}(\mathbf{v})$ to $\tilde{\mathbf{C}}(\omega)$.
- 3 Calculate filter $\tilde{\mathbf{K}}(\omega)$ using Eq.(39).
- 4 Sample a random Gaussian white noise field $\mathbf{z}(\mathbf{p})$.

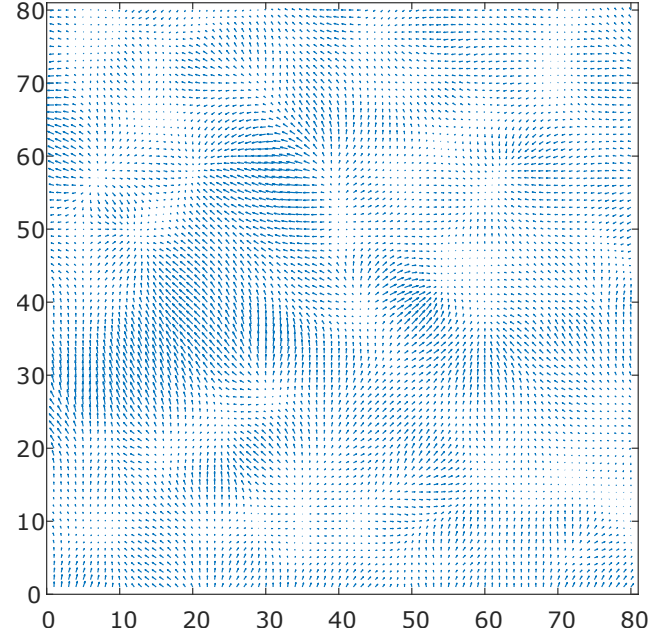


Figure 9: Part of a random distortion vector field $\mathbf{e}(\mathbf{p})$, derived from the autocorrelation function shown in Figs. 6,7. This is a simulated turbulence-induced distortion. For clarity, this plot zooms-in on a 80×80 pixel sub-domain of the image

- 5 Fourier transform $\mathbf{z}(\mathbf{p})$ to $\tilde{\mathbf{z}}(\omega)$.
- 6 Use $\tilde{\mathbf{K}}(\omega)$ in a simple multiplication per ω , as written in Eq. (36), to obtain $\tilde{\mathbf{e}}(\omega)$.
- 7 Inverse Fourier transform $\tilde{\mathbf{e}}(\omega)$, to obtain the distortion field $\mathbf{e}(\mathbf{p})$, of variance 1.
- 8 Amplify $\mathbf{e}(\mathbf{p})$ so its variance is consistent with Eq. (1).

For example, Fig. 9 plots a field $\mathbf{e}(\mathbf{p})$ created by this recipe, in correspondence with the autocorrelation and kernel functions shown in Figs. 6,7,8. The plot in Fig. 9 zooms on a 80×80 pixel sub-domain of the image, for clarity.

6. Practical Considerations

In practice, a computer does not perform a continuous Fourier transform, but a discrete, fast Fourier transform (FFT). This has several implications. In a square grid, the spatial locations and frequencies are sampled. Using FFT as in steps 2, 5 above induces a multiplicative scale relative to a continuous-domain Fourier transform that is sampled. This factor is compensated for: in step 7 the field is amplified to have unit variance.

Moreover, FFT is cyclic: elements in one side of its input affect the other side. This wrap-around can cause problems in functions that do not spatially decay fast enough. As seen in Fig 4, b_{\perp} may decay very slowly. Despite having very low values at the periphery, wrap-around issues produce negative oscillations in the Fourier domain that render

Table 1: Parameters of our examples

Example	C_n^2 [m ^{-2/3}]	L [km]	f [mm]	$f\#$	h [m]
Fig. 10	$3.6 \cdot 10^{-13}$	2.0	300	5.6	4
Fig. 11	$3.6 \cdot 10^{-13}$	1.3	380	5.6	4
Fig. 12	$3.6 \cdot 10^{-13}$	2.0	200	3.2	20

the supposedly positive spectral density invalid. This can be mitigated by extending the spatial domain, at a higher computational cost. In practice, we feathered $\mathbf{C}(\mathbf{v})$ using a Blackman window that spans the domain of \mathbf{v} .

7. Using the Distortion Field

A source turbulence-free image is $g_{\text{raw}}(\mathbf{p})$, where \mathbf{p} is rectified on a regular grid. Due to turbulence, any pixel location \mathbf{p} is displaced to $\mathbf{p} + \mathbf{e}(\mathbf{p})$, creating the set of values on a nonuniform grid

$$g_{\text{nonuniform}}(\mathbf{p} + \mathbf{e}(\mathbf{p})) = g_{\text{raw}}(\mathbf{p}) . \quad (40)$$

The eventual distorted image $g_{\text{distorted}}(\mathbf{p})$ is rendered by interpolating $g_{\text{nonuniform}}(\mathbf{p} + \mathbf{e}(\mathbf{p}))$ to the uniform pixel grid. For example, Fig. 10[Top] represents an undistorted view, $g_{\text{raw}}(\mathbf{p})$. Since Fig. 10[Top] is in color, we first calculated $\gamma(q)$ for $\lambda = 450, 550, 650\text{nm}$. Practically, we saw that $\gamma(q)$ is insensitive to λ in visible light, thus a single random distortion field applies to all color channels. Based on the example parameters that lead to Figs. 6,7,8,9, we rendered a distorted image, $g_{\text{distorted}}(\mathbf{p})$, shown in Fig. 10[Bottom].

We show additional examples. They use most parameter values as in the example detailed in Sec. 4.3. The parameters that were changed are detailed in Table 1. Correspondingly, the results are shown in Figs. 11 and 12. Specifically, in Fig. 11, the focal length and object range changed to $f = 380\text{mm}$ and $L = 1.3\text{km}$, respectively. The distortion variance in pixel units is nearly the same, but the correlation-range doubles. Hence, distortions have lower spatial frequencies, yet similar amplitude. The process was then run on a new random white noise field $\mathbf{z}(\mathbf{p})$ in step 4.

8. Verification

It is possible to verify empirically that distortion statistics are consistent with the theory. Let us render N distortion fields, $\{\mathbf{e}_i(\mathbf{p})\}_{i=1}^N$, each based on a different sampled white noise field, in step 4 above. An empirical version of Eqs. (24,25) is

$$\begin{aligned} \hat{C}_{\parallel}(\mathbf{v}) &= \frac{1}{N|\Lambda|} \sum_{i=1}^N \sum_{\mathbf{p} \in \Lambda} \hat{\mathbf{v}}^T \mathbf{e}_i(\mathbf{p}) \mathbf{e}_i^T(\mathbf{p} + \mathbf{v}) \hat{\mathbf{v}} \\ \hat{C}_{\perp}(\mathbf{v}) &= \frac{1}{N|\Lambda|} \sum_{i=1}^N \sum_{\mathbf{p} \in \Lambda} \hat{\mathbf{v}}^T \mathbf{R}^T \mathbf{e}_i(\mathbf{p}) \mathbf{e}_i^T(\mathbf{p} + \mathbf{v}) \mathbf{R} \hat{\mathbf{v}}, \end{aligned} \quad (41)$$

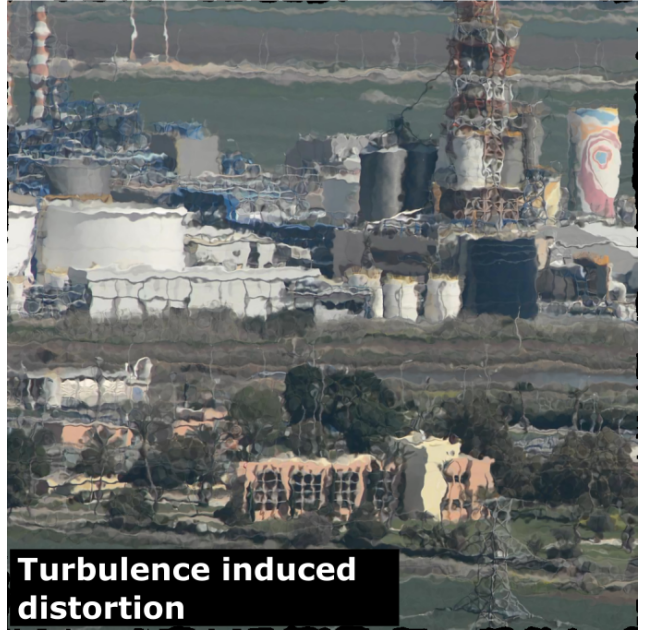


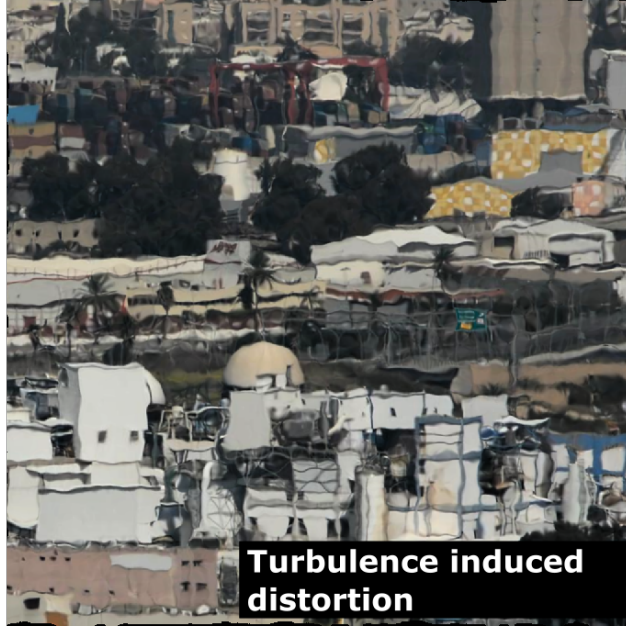
Figure 10: [Top] A raw source 1024×1024 image, without random distortion. [Bottom] The image after undergoing distortion consistent with turbulence. Part of the distortion field is shown in Fig. 9. This distortion was derived from the autocorrelation function shown in Figs. 6,7.

where Λ is a random subset of pixels.

Continuing with the example described in Figs. 6, 7, 8, we rendered $N = 1500$ distortion fields, as the one in Fig. 9. We used horizontal \mathbf{v} vectors and $|\Lambda| = 100$. From Eqs.



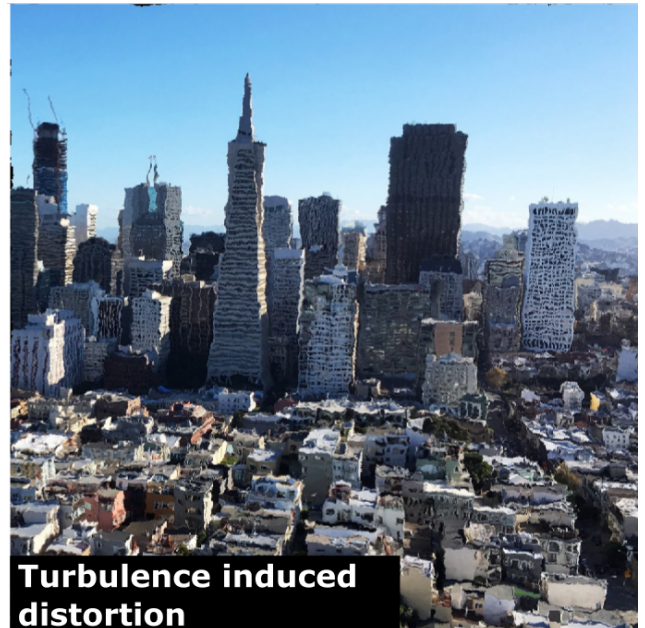
Raw source image



Turbulence induced distortion



Raw source image



Turbulence induced distortion

Figure 11: [Top] A raw source 1024×1024 image, $g_{\text{raw}}(\mathbf{p})$, without random distortion. [Bottom] $g_{\text{distorted}}(\mathbf{p})$, the image after undergoing distortion consistent with turbulence. The parameters are described in Sec. 4.3 and Table 1. Here 2D spatial correlations of the distortion field have about twice the pixel-range, compared to Fig. 10. Hence, the turbulence-distortion field is smoother here.

(10,16)

$$\eta = \frac{\theta}{\theta_D} = \frac{|\mathbf{v}|}{f\theta_D}. \quad (42)$$

Using Eqs. (41,42), $\hat{C}_{\parallel}(\mathbf{v})$, $\hat{C}_{\perp}(\mathbf{v})$ are converted to $\hat{b}_{\parallel}(\eta)$,

Figure 12: [Top] A raw source 1024×1024 image, $g_{\text{raw}}(\mathbf{p})$. Photo courtesy of [<http://pixabay.com>]. [Bottom] $g_{\text{distorted}}(\mathbf{p})$, the image after undergoing distortion consistent with turbulence. The parameters are described in Sec. 4.3 and Table 1.

$\hat{b}_{\perp}(\eta)$. Figure 13 compares the empirical \hat{b}_{\parallel} , \hat{b}_{\perp} to the theoretical b_{\parallel} , b_{\perp} . From Fig. 13, generally, there is very good consistency between the theoretical AA correlation and our rendered fields. For high $|\mathbf{v}|$, i.e. η , the empirical correlation is a little smaller than the theoretical one. We believe this is because of the FFT wrap-around, whose repercus-

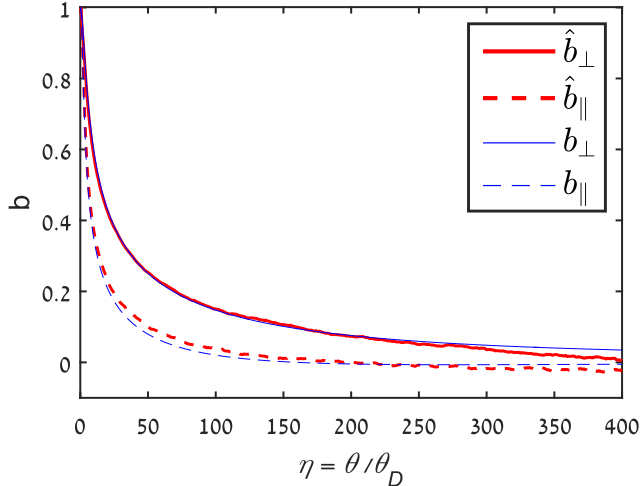


Figure 13: Plot of the empirical $\hat{b}_{\parallel}(\eta)$ and $\hat{b}_{\perp}(\eta)$, using $N = 1500$ fields, $|\Lambda| = 100$ random pixels and setup parameters as detailed in Sec. 4.3. The results are compared to the theoretical correlations $b_{\parallel}(\eta)$ and $b_{\perp}(\eta)$.

sions are discussed in Sec. 6. A wrap-around has a higher deterioration effect as a vector $\mathbf{p} + \mathbf{v}$ is closer to the image boundary, i.e. at large $|\mathbf{v}|$.

9. Discussion of Generalizations

The recipe we give is by no means the only possible one. For example, Fourier domain processing can be bypassed: the kernel $\mathbf{K}(\mathbf{p})$ can be derived in Eq. (35) using other deconvolution methods, and then be applied in the spatial domain (34). It should be beneficial to explore such variations.

This work focused on a particular turbulence-induced image effect: distortion in a 2D image, that views a scene via a stationary turbulent field. This approach may be extended, to express other turbulence-induced image effects:

- Turbulence creates image blur [9, 21, 23]. As distortion, blur is a 2D operation on a 2D image. Similarly to distortion, blur parameters form a vector, e.g. widths of the blur kernel in two components. Moreover, the turbulence-induced blur-parameter field is random, having correlation between adjacent points. There are closed-form physical models for the blur that can result from turbulence. Hence, we believe that a similar recipe can be devised for rendering random 2D blur fields that are consistent with turbulence. The same hypothesis applies to turbulence-induced scintillation.

- Turbulence is dynamic, and so are its image effects. The 2D distortion field is correlated both in 2D and in time. To render videos, a physics-based spatiotemporal correlation

function should be incorporated.

- In some cases, the turbulence field is not spatially stationary. Specifically, oblique views in steep angles as in astronomy pass through atmospheric layers having significant spatial variations of \mathcal{C}_n^2 . Extending the approach to such cases is important. It may be aided by assumptions that are often used in astronomy, based on a layered structure.

Acknowledgments

We thank Johanan Erez, Ina Talmon, Dani Yagodin for technical support. Yoav Schechner is a Landau Fellow - supported by the Taub Foundation. The work was supported by the Israel Science Foundation (ISF Grant 1467/12). This work was conducted in the Ollendorff Minerva Center. Minerva is funded through the BMBF. Part of this work was conducted while Armin Schwartzman and Marina Alterman were with the Faculty of Electrical Engineering, Technion.

References

- [1] M. Alterman, Y. Y. Schechner, M. Vo and S. G. Narasimhan. Passive tomography of turbulence strength. In *Proc. ECCV*, pages 47-60, 2014.
- [2] M. Alterman, Y. Swirski and Y. Schechner. STELLA MARIS: Stellar marine refractive imaging sensor. In *Proc. IEEE ICCP*, 2014.
- [3] D. Akkaynak, T. Treibitz, T. Shlesinger, R. Tamir, Y. Loya, and D. Iluz. What is the space of attenuation coefficients in underwater computer vision? In *Proc. CVPR*, 2017.
- [4] L. C. Andrews and R. L. Phillips. *Laser Beam Propagation Through Random Media*. volume 52. SPIE press Bellingham, WA, 2005.
- [5] B. Atcheson, W. Heidrich and I. Ihrke. An evaluation of optical flow algorithms for background oriented Schlieren imaging. *Experiments in Fluids* 46(3), 467-476, 2009.
- [6] B. Atcheson, I. Ihrke, W. Heidrich, A. Tevs, D. Bradley, M. Magnor, H. P. Seidel. Time-resolved 3D capture of non-stationary gas flows. *ACM TOG* 27(5), 132:1-132:9, 2008.
- [7] M. S. Belen’kii, J. M. Stewart, and P. Gillespie. Turbulence-induced edge image waviness: theory and experiment. *Applied Optics*, 40(9):1321-1328, 2001.
- [8] D. Berman, T. Treibitz and S. Avidan. Air-light estimation using haze-lines. In *Proc. ICCP*, 2017.
- [9] T. Bishop and P. Favaro. Blind deconvolution. In *Encyclopedia of Computer Vision*, pages 52-57. Springer, 2014.
- [10] Y. Cheon and A. Muschinski. Closed-form approximations for the angle-of-arrival variance of plane and spherical waves propagating through homogeneous and isotropic turbulence. *JOSA A*, 24(2):415-422, 2007.
- [11] Y. Chuang, D. E. Zongker, J. Hindorff, B. Curless, D. H. Salesin, and R. Szeliski. Environment matting extensions: Towards higher accuracy and real-time capture. In *ACM Siggraph*, pages 121-130, 2000.

- [12] J. H. Churnside and R. J. Lataitis. Angle-of-arrival fluctuations of a reflected beam in atmospheric turbulence. *JOSA A*, 4(7):1264–1272, 1987.
- [13] S. Dong, T. Haist, W. Osten, T. Ruppel, and O. Sawodny. Response analysis of holography-based modal wavefront sensor. *Applied Optics*, 51(9):1318–1327, 2012.
- [14] B. Fishbain, L. P. Yaroslavsky, and I. A. Ideses. Real-time stabilization of long range observation system turbulent video. *Journal of Real-Time Image Processing*, 2(1):11–22, 2007.
- [15] G. Potvin, J. L. Forand and D. Dion. A parametric model for simulating turbulence effects on imaging systems. *Defense Research and Development Canada (DRDC) Valcartier Technical Report 2006-787*, 2007.
- [16] I. Gkioulekas, S. Zhao, K. Bala, T. Zickler, and A. Levin. Inverse volume rendering with material dictionaries. *ACM TOG*, 32(6):162, 2013.
- [17] E. Grossman, R. Tzioni, A. Gur, E. Gur, and Z. Zalevsky. Optical through-turbulence imaging configuration: experimental validation. *Optics Letters*, 35(4):453–455, 2010.
- [18] M. Gupta and S. G. Narasimhan. Legendre fluids: a unified framework for analytic reduced space modeling and rendering of participating media. In *Proc. ACM SIGGRAPH/Eurographics Symposium on Computer Animation*, pages 17–25, 2007.
- [19] D. Gutierrez, A. Munoz, O. Anson, and F. J. Seron. Non-linear volume photon mapping. In *Rendering Techniques*, pages 291–300, 2005.
- [20] D. Gutierrez, F. J. Seron, A. Munoz, and O. Anson. Simulation of atmospheric phenomena. *Computers & Graphics*, 30(6):994–1010, 2006.
- [21] S. Harmeling, M. Hirsch, S. Sra, and B. Schölkopf. Online blind deconvolution for astronomy. In *Proc. IEEE ICCP*, 2009.
- [22] F. Heide, L. Xiao, A. Kolb, M. B. Hullin, and W. Heidrich. Imaging in scattering media using correlation image sensors and sparse convolutional coding. *Optics Express*, 22(21):26338–26350, 2014.
- [23] J. Holloway, S. Asif, M. Sharma, N. Matsuda, R. Horstmeyer, O. Cossairt, and A. Veeraraghavan. Toward long distance, sub-diffraction imaging using coherent camera arrays. *IEEE T. Computational Photography* 2(3):251 - 265, 2016.
- [24] R. Horisaki, R. Takagi, and J. Tanida. Learning-based imaging through scattering media. *Optics Express*, 24(13):13738–13743, 2016.
- [25] M. B. Hullin, M. Fuchs, I. Ihrke, H.-P. Seidel, and H. P. Lensch. Fluorescent immersion range scanning. *ACM TOG*, 27(3):87, 2008.
- [26] I. Ihrke, G. Ziegler, A. Tevs, C. Theobalt, M. Magnor, and H. P. Seidel. Eikonal rendering: Efficient light transport in refractive objects. In *ACM TOG*, 26(3):59, 2007.
- [27] Y. Ji, J. Ye, and J. Yu. Reconstructing gas flows using light-path approximation. In *Proc. IEEE CVPR*, pages 2507–2514, 2013.
- [28] N. Joshi, M. F. Cohen. Seeing Mt. Rainier: Lucky imaging for multi-image denoising, sharpening, and haze removal. In *Proc. IEEE ICCP*, 2010.
- [29] J. Kim, D. Lanman, Y. Mukaigawa, and R. Raskar. Descattering transmission via angular filtering. In *Proc. ECCV*, pages 86–99, 2010.
- [30] A. N. Kolmogorov. Dissipation of energy in locally isotropic turbulence. In *Dokl. Akad. Nauk SSSR*, volume 32, pages 16–18. JSTOR, 1941.
- [31] A. N. Kolmogorov. The local structure of turbulence in incompressible viscous fluid for very large reynolds numbers. In *Dokl. Akad. Nauk SSSR*, volume 30, pages 301–305. JSTOR, 1941.
- [32] N. S. Kopeika, *A System Engineering Approach to Imaging*. SPIE Press, 1998.
- [33] R. G. Lane, A. Glindemann, and L. C. Dainty. Simulation of a Kolmogorov phase screen. *Waves in Random media*, 2(3):209–224, 1992.
- [34] B. W. Levinger. The square root of a 2×2 matrix. *Mathematics Magazine*, 53(4):222–224, 1980.
- [35] A. Levis, Y. Y. Schechner and A. B. Davis. Multiple-scattering microphysics tomography. In *Proc. IEEE CVPR*, 2017.
- [36] H. Y. Liu, E. Jonas, L. Tian, J. Zhong, B. Recht, and L. Waller. 3D imaging in volumetric scattering media using phase-space measurements. *Optics Express*, 23(11):14461–14471, 2015.
- [37] C. Ma, X. Lin, J. Suo, Q. Dai, and G. Wetzstein. Transparent object reconstruction via coded transport of intensity. In *Proc. IEEE CVPR* 3238–3245, 2014.
- [38] H. Ma, Z. Y. X. Wang, Y. Ma, P. Zhou, X. Xu, and Z. Liu. Adaptive conversion of a wavefront-distortion beam to near-diffraction-limited flat-top beam based on stochastic parallel gradient descent algorithm. In *Proc. SPIE Photonics Asia 2010*, pages 78430P–78430P, 2010.
- [39] M. Mendillo, S. Laurent, J. Wilson, J. Baumgardner, J. Konrad, and W. C. Karl. The sources of sodium escaping from io revealed by spectral high definition imaging. *Nature*, 448(7151):330–332, 2007.
- [40] D. Miyazaki, M. Saito, Y. Sato, and K. Ikeuchi. Determining surface orientations of transparent objects based on polarization degrees in visible and infrared wavelengths. *JOSA A*, 19(4):687–694, 2002.
- [41] S. G. Narasimhan, S. K. Nayar, B. Sun, and S. J. Koppal. Structured light in scattering media. In *Proc. IEEE ICCV*, pages 420–427, 2005.
- [42] M. O’Toole, J. Mather, and K. N. Kutulakos. 3D shape and indirect appearance by structured light transport. In *Proc. IEEE CVPR*, pages 3246–3253, 2014.
- [43] E. Repasi and R. Weiss. Computer simulation of image degradations by atmospheric turbulence for horizontal views. In *Proc. SPIE Defense, Security, and Sensing*, pages 80140U–80140U, 2011.
- [44] M.C., Roggemann, B. Welsh, *Imaging Through Turbulence*, CRC Press, 1996.
- [45] A. Sedlazeck, K. Koser, R. Koch, 3D reconstruction based on underwater video from ROV Kiel 6000 considering underwater imaging conditions. In *Proc. IEEE OCEANS EU-ROPE*, 2009.

[46] M. Sheinin and Y. Y. Schechner. The next best underwater view. In *Proc. IEEE CVPR*, 2016.

[47] F. J. Serón, D. Gutierrez, G. Gutierrez, and E. Cerezo. Implementation of a method of curved ray tracing for inhomogeneous atmospheres. *Computers & Graphics*, 29(1):95–108, 2005.

[48] M. Shimizu, S. Yoshimura, M. Tanaka, M. Okutomi, Super-resolution from image sequence under influence of hot-air optical turbulence. In *Proc. IEEE CVPR*, 2008.

[49] O. Spier, T. Treibitz and G. Gilboa. In situ target-less calibration of turbid media. In *Proc. IEEE ICCP*, 2017.

[50] J. Stam and E. Fiume. Turbulent wind fields for gaseous phenomena. *ACM Siggraph* pages 369–376, 1993.

[51] J. Stone, P. Hu, S. Mills, and S. Ma. Anisoplanatic effects in finite-aperture optical systems. *JOSA A*, 11(1):347–357, 1994.

[52] V. I. Tatarskii. *Wave Propagation in a Turbulent Medium*. McGraw-Hill, 1961.

[53] Y. Tian, S. Narasimhan and A. Vannevel. Depth from optical turbulence. In *Proc. IEEE CVPR*, 2012.

[54] B. Trifonov, D. Bradley, W. Heidrich. Tomographic reconstruction of transparent objects. In *Proc. Eurographics Symposium on Rendering*, 51–60, 2006.

[55] A. T. Watnik and P. S. Lebow. Weak-signal iterative holography. *Applied Optics*, 54(10):2615–2619, 2015.

[56] G. Wetzstein, D. Roodnick, W. Heidrich, and R. Raskar. Refractive shape from light field distortion. In *Proc. IEEE ICCV*, pages 1180–1186, 2011.

[57] T. Xue, M. Rubinstein, N. Wadhwa, A. Levin, F. Durand, and W. T. Freeman. Refraction wiggles for measuring fluid depth and velocity from video. In *Proc. ECCV*, pages 767–782, 2014.

[58] S. K. Yeung, C. K. Tang, M. S. Brown, and S. B. Kang. Mating and compositing of transparent and refractive objects. *ACM TOG*, 30(1):2, 2011.

[59] Z. Yu, T. Qiuyan, W. Jin, and S. Quan. Numerical simulator of atmospherically distorted phase screen for multibeam time-dependent scenario. *Applied Optics*, 53(22):5008–5015, 2014.

[60] X. Zhu and P. Milanfar. Stabilizing and deblurring atmospheric turbulence. In *Proc. IEEE ICCP*, 2011.

[61] X. Zhu and P. Milanfar. Removing atmospheric turbulence via space-invariant deconvolution. *IEEE T. PAMI*, 35(1):157–170, 2013.

Table of notations	
A	A coefficient function of the autocorrelation matrix
a	Parameter of ${}_2F_1()$
AA	Angle of arrival
b	AA correlation
b_{\perp}	b component perpendicular to plane Π
b_{\parallel}	b component parallel to plane Π
\hat{b}_{\perp}	Empirical b_{\perp}
\hat{b}_{\parallel}	Empirical b_{\parallel}
B	A coefficient function of the autocorrelation matrix
β	A coefficient that equals 0.5216
\mathbf{C}	Matrix valued autocorrelation function
$\tilde{\mathbf{C}}$	Spatial Fourier transform of \mathbf{C}
C_{xx}	Correlation of the horizontal components of field \mathbf{e}
C_{xy}	Correlation of the horizontal and vertical components of field \mathbf{e}
C_{yx}	Correlation of the vertical and horizontal components of field \mathbf{e}
C_{yy}	Correlation of the vertical components of field \mathbf{e}
c	Parameter of ${}_2F_1()$
C_n^2	Turbulence structure constant
\mathbf{Cov}	The covariance operation
D	Diameter of the camera lens.
d	Parameter of ${}_2F_1()$
\mathbf{e}	A random vector field
e_{\perp}	Field component perpendicular to plane Π
e_{\parallel}	Field component parallel to plane Π
$\tilde{\mathbf{e}}$	Spatial Fourier transform of \mathbf{e}
E	Expectation
η	Normalized inter-object view angle
f	Focal length of the camera
${}_2F_1()$	Hypergeometric function
g_{raw}	Source turbulence-free image
$g_{distorted}$	Image distorted by turbulence
$g_{nonuniform}$	g_{raw} on nonuniform grid, created by turbulence
γ	AA variance coefficient
Γ	Gamma function
h	Height above ground
H	An integrated function to derive b_{\perp} and b_{\parallel}
i	Index of distortion field
\mathbf{I}	Identity matrix
j	$\sqrt{-1}$
J_0, J_2	Bessel functions of the first kind
\mathbf{K}	Matrix valued kernel field
$\tilde{\mathbf{K}}$	Spatial Fourier transform of \mathbf{K}
\tilde{K}_{xx}	First row and first column component of $\tilde{\mathbf{K}}$
\tilde{K}_{xy}	First row and second column component of $\tilde{\mathbf{K}}$
\tilde{K}_{yx}	Second row and first column component of $\tilde{\mathbf{K}}$
\tilde{K}_{yy}	Second row and second column component of $\tilde{\mathbf{K}}$
κ	Integration parameter
l_0	Turbulence inner scale
L_0	Turbulence outer scale
L	Distance between the camera and the object

Continuation of table of notations

λ	Light wavelength
Λ	Random subset of pixels
M_η	An integrated function to derive b_\perp and b_\parallel
m	Summation index in ${}_2F_1()$
μ	Parameter of Γ
N	Number of distortion fields
o, o'	object points
\mathbf{o}, \mathbf{o}'	Unit vectors of lines of sight to o, o' , respectively
$\boldsymbol{\omega}$	2D spatial frequency vector
\mathbf{p}	Pixel location vector
Π	A plane defined by \mathbf{o}, \mathbf{o}'
q	Fresnel number
Q	An integrated function to derive b_\perp and b_\parallel
r	The length $ \mathbf{v} $
\mathbf{R}	Rotation matrix
ρ	Normalized outer scale
s	Frequency domain scalar function
σ_{AA}^2	AA variance
t	Frequency domain scalar function
\mathbf{T}	Transposition operation
θ	Inter-object view angle
θ_D	Angular size of the aperture, from the object's point of view
U	Spatial image size
\mathbf{v}	Vector between pixels to which \mathbf{o}, \mathbf{o}' are projected without distortion
W	Number of object points
(x, y)	Cartesian coordinates
ξ	Dimensionless parameter
\mathbf{z}	White noise vector field
ζ	Parameter of ${}_2F_1()$
$\tilde{\mathbf{z}}$	Spatial Fourier transform of \mathbf{z}